

Centroid–moment tensor inversions using high-rate GPS waveforms

Thomas B. O'Toole,¹ Andrew P. Valentine² and John H. Woodhouse¹

¹Department of Earth Sciences, University of Oxford, South Parks Road, Oxford, OX1 3AN, UK. E-mail: thomas.otoole@earth.ox.ac.uk

²Department of Earth Sciences, Universiteit Utrecht, PO Box 80021, 3508TA Utrecht, the Netherlands

Accepted 2012 July 9. Received 2012 June 6; in original form 2012 April 18

SUMMARY

Displacement time-series recorded by Global Positioning System (GPS) receivers are a new type of near-field waveform observation of the seismic source. We have developed an inversion method which enables the recovery of an earthquake's mechanism and centroid coordinates from such data. Our approach is identical to that of the 'classical' Centroid–Moment Tensor (CMT) algorithm, except that we forward model the seismic wavefield using a method that is amenable to the efficient computation of synthetic GPS seismograms and their partial derivatives. We demonstrate the validity of our approach by calculating CMT solutions using 1 Hz GPS data for two recent earthquakes in Japan. These results are in good agreement with independently determined source models of these events. With wider availability of data, we envisage the CMT algorithm providing a tool for the systematic inversion of GPS waveforms, as is already the case for teleseismic data. Furthermore, this general inversion method could equally be applied to other near-field earthquake observations such as those made using accelerometers.

Key words: Satellite geodesy; Earthquake ground motions; Earthquake source observations; Computational seismology; Theoretical seismology; Early warning.

1 INTRODUCTION

The determination of earthquake source parameters is a fundamental problem in seismology. The Centroid–Moment Tensor (CMT) method of Dziewonski *et al.* (1981) is one of the most robust techniques that has been developed for obtaining the location and mechanism of a seismic event; it has been routinely applied to the inversion of teleseismic waveforms for over 30 years, and underpins the ongoing Global CMT project (www.globalcmt.org). Recently, a new type of near-field waveform data has become available to seismologists: high-rate Global Positioning System (HRGPS) measurements of ground displacements (Larson *et al.* 2003). In this paper, we investigate the possibility of using 1 Hz GPS data in CMT inversions to recover the moment tensor and spatio-temporal location of an earthquake.

The present work is made possible by the increasing availability of high-quality GPS data to seismologists. The versatility of GPS as a tool to measure Earth's deformation at timescales ranging from seconds to years has meant that permanent GPS networks are now routinely deployed in tectonically active regions. Such networks, typically operating at 1 Hz sampling rates, will capture local seismicity regardless of their original observational purpose. Furthermore—partly in response to the demands of seismologists (Hammond *et al.* 2010)—data acquisition, storage and processing systems have become more sophisticated over time so that state of the art GPS networks are now able to stream 10 Hz data, yielding displacement waveforms with millimetre-level accuracy in real-

time (Bock *et al.* 2011). This potentially rich data resource is yet to be fully exploited, and so there is a need to develop methods for the routine analysis of HRGPS waveforms; the CMT algorithm is a strong candidate since it is well understood and accepted for teleseismic and regional data (e.g. Dziewonski *et al.* 1983; Pondrelli *et al.* 2002).

GPS networks have been used to make many observations of dynamic displacements caused by earthquakes (e.g. Nikolaidis *et al.* 2001; Kouba 2003; Davis & Smalley 2009; Shi *et al.* 2010; O'Toole & Woodhouse 2011; Bock *et al.* 2011). However, such data have only been used to construct source models for a handful of events: the 2003 Tokachi–Oki earthquake (Miyazaki *et al.* 2004), the 2003 San Simeon earthquake (Ji *et al.* 2004), the 2005 Fukuoka earthquake (Kobayashi *et al.* 2006), the 2008 Iwate–Miyagi earthquake (Yokota *et al.* 2009), the 2008 L'Aquila earthquake (Avallone *et al.* 2011), the 2010 Maule earthquake (Delouis *et al.* 2010; Vigny *et al.* 2011) and the 2011 Tohoku earthquake (Ammon *et al.* 2011; Yue & Lay 2011). All of these studies inverted HRGPS data to obtain a kinematic rupture model of the earthquake on a finite fault of assumed location, size and orientation. The application of GPS data presented here differs from these earlier studies as we solve for the optimal long-period description of an earthquake without making any *a priori* assumption about the location or mechanism.

Several characteristics of HRGPS time-series make them suitable for inversion using the CMT algorithm. The fact that GPS receivers measure displacement directly means that they record waveforms

that are inherently rich in long-period information. Indeed since GPS receivers capture the permanent 'static' displacement caused by an earthquake, they are actually sensitive to frequencies down to 0 Hz. Furthermore, Bock *et al.* (2004) showed that GPS receivers can detect arbitrarily large ground displacements without clipping. As a consequence GPS receivers are, in effect, long-period–strong-motion displacement seismometers. Since the CMT method requires long-period, long-wavelength data to justify its parameterization of an earthquake as a point source, HRGPS data should be well suited to an inversion within the CMT framework. Of course, when compared to teleseismic observations, finite fault effects will be more significant in the near-field. However for the earthquakes examined in this report, we find that rupture complexity does not preclude the stable recovery of a CMT solution from low-pass filtered HRGPS waveforms.

Ultimately, we would like to improve our sampling of the seismic displacement field in both space and frequency through simultaneous inversion of seismic and geodetic earthquake observations (e.g. Lay 2011). The CMT inversion formulation is well suited to a straightforward implementation of joint inversions, and so a first step towards this aim is to carry out inversions of HRGPS waveforms alone. Furthermore, since the CMT approach is general it may also be applied to other near-field seismic observations, provided that instruments remain on-scale during an earthquake and are sensitive to long-period ground motions. The use of these new and independent types of data within the CMT inversion framework may be of great value in quantifying and reducing uncertainties in earthquake source parameters determined using long-period teleseismic data.

We follow the approach of Dziewonski *et al.* (1981) to retrieve the six independent components of the moment tensor plus the spatio-temporal position of the earthquake's centroid from HRGPS data. Starting at a reference source time and location—the hypocentre obtained from *P*-wave arrival times, for example—we invert for an initial moment tensor. Subsequently, we solve iteratively for the correction to this original source mechanism, location and origin time which minimizes the least-squares misfit between HRGPS data and corresponding synthetics. At each iteration, the value of the perturbation is evaluated using so-called 'kernel functions': partial derivatives of the synthetic waveforms with respect to the 10 source parameters.

In this paper, we extend the work of O'Toole & Woodhouse (2011) to compute accurate derivative kernels for synthetic GPS seismograms, allowing us to invert HRGPS data for an earthquake's CMT solution. To validate our approach, we perform test inversions of synthetic 1 Hz GPS data sets. Using this new method, we obtain CMT solutions for two moderate sized earthquakes that were well observed by GPS instruments in Japan.

2 THEORY: CMT INVERSIONS

For completeness, we begin by briefly summarizing the CMT algorithm; for a detailed description of the method as originally conceived for long-period teleseismic waveform data, see Dziewonski *et al.* (1981), Dziewonski & Woodhouse (1983a) and Dziewonski & Woodhouse (1983b). In the following, we use the word 'seismogram' generally to describe any functional of the seismic source for which observations and forward modelling methods exist since any such data could, in principle, be used in inversions for earthquake source parameters; in the present context a seismogram is a high-rate GPS waveform.

2.1 Linear inversion: the moment tensor at an assumed centroid location

An indigenous source such as an earthquake is required to exert no net force or torque on the Earth. Supposing that the location of a seismic event is known in time t and space \mathbf{x} , we can completely specify the source, \mathbf{f} , in terms of the six independent elements of a symmetric moment tensor \mathbf{M} (e.g. Dziewonski & Woodhouse 1983b)

$$\mathbf{f} = (M_{rr}, M_{\theta\theta}, M_{\phi\phi}, M_{r\theta}, M_{r\phi}, M_{\theta\phi})^T. \quad (1)$$

The forward problem for the predicted waveforms arising from such a source located at \mathbf{x}_s can be written (Gilbert & Dziewonski 1975)

$$u_k(\mathbf{x}, t) = \sum_{i=1}^6 \psi_{ki}(\mathbf{x}, \mathbf{x}_s, t) f_i. \quad (2)$$

The k th seismogram in the data set, u_k , is given by a linear combination of the so-called excitation kernels, ψ_{ki} , weighted by the source vector. These kernel functions, the partial derivatives of the seismogram with respect to the components of \mathbf{f} , represent the response excited by unit sources corresponding to each independent component of the moment tensor, and so also depend on the assumed earth model.

Our problem is then to estimate \mathbf{f} , given a set of observed seismograms \mathbf{d} . From (2), we must solve a linear inverse problem of the form

$$\mathbf{A}\mathbf{f} = \mathbf{d}, \quad (3)$$

where \mathbf{A} is a matrix of excitation kernels calculated for all the seismograms contained in the data vector. Generally we have many more data than the six unknown components of \mathbf{f} , so we seek the source that minimizes the least-squares misfit, m^2 , between data and the corresponding synthetic seismograms \mathbf{s}

$$m^2 = \frac{(\mathbf{d} - \mathbf{s})^T(\mathbf{d} - \mathbf{s})}{\mathbf{d}^T \mathbf{d}}, \quad (4)$$

which can be shown (see, e.g. Menke 1989) to lead to the solution

$$\mathbf{f} = (\mathbf{A}^T \mathbf{A})^{-1} \mathbf{A}^T \mathbf{d}. \quad (5)$$

Given some estimate of the source location—for example, the hypocentre as determined from *P*-wave arrival times—we can use this linear inversion scheme to obtain the moment tensor. Within the limitations of this source representation, the solution is exact, and convergence is reached after a single iteration.

2.2 Non-linear inversion: retrieval of all 10 source parameters from waveform data

Since the source location assumed in Section 2.1 may not correspond to the position of the earthquake's centroid, we should actually determine the location of the earthquake in space and time in addition to the moment tensor, which requires the solution of a non-linear inverse problem. In this case, the source vector \mathbf{f} has 10 components

$$\mathbf{f} = (M_{rr}, M_{\theta\theta}, M_{\phi\phi}, M_{r\theta}, M_{r\phi}, M_{\theta\phi}, \theta_c, \phi_c, z_c, t_c)^T, \quad (6)$$

where the centroid latitude, longitude and depth are given by (θ_c, ϕ_c, z_c) and t_c is the centroid time. Since non-linearity is weak, we can linearize the problem and perform an iterative least-squares inversion for the best-fitting point source via

$$\mathbf{f}_{i+1} = \mathbf{f}_i + (\mathbf{A}_i^T \mathbf{A}_i)^{-1} \mathbf{A}_i^T (\mathbf{d} - \mathbf{s}_i), \quad (7)$$

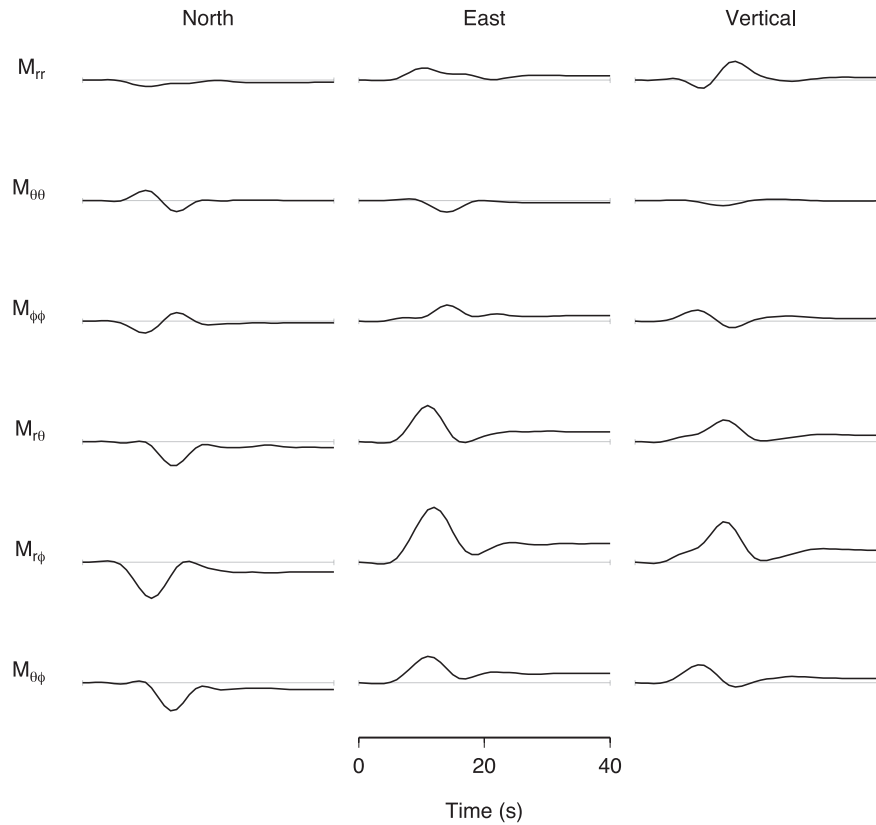


Figure 1. An example set of GPS excitation kernels computed for a station located at a distance of 39.6 km and azimuth 118.2° for an earthquake with a depth of 35 km. These six traces represent the ground motion excited by unit sources corresponding to each individual component of the moment tensor. The synthetic seismogram for a particular component of ground motion is then a linear combination of the six traces, weighted by the moment tensor. The CMT algorithm allows us to determine the optimum moment tensor by minimizing the difference between HRGPS data and synthetics. The earth model used in this calculation is given in Table 1. The vertical scale is common to all the seismograms.

where \mathbf{A} now includes the location kernels $\partial_{\theta_c} u_k$, $\partial_{\phi_c} u_k$, $\partial_{z_c} u_k$ and $\partial_{t_c} u_k$, and the subscript i is included to emphasize the quantities which depend on \mathbf{f} and must be recalculated at each iteration. The starting source, \mathbf{f}_0 , is typically the result of the linear inversion described in Section 2.1.

2.3 Calculation of synthetic seismograms and their partial derivatives

The calculation of excitation and location kernels appropriate to a particular type of data is a prerequisite for applying the foregoing theory to the inversion of those data. The CMT algorithm uses normal mode summation to compute long-period teleseismic waveform synthetics and their partial derivatives. While we could also use normal mode summation to compute synthetic GPS waveforms, it is unlikely to be the best choice for the application presented here. Apart from the well-known problem of computing mode catalogues at frequencies higher than about 100 mHz (e.g. Yang *et al.* 2010) the construction of whole earth eigenfunctions is computationally expensive for near-field data. Furthermore, we would like to compute kernels using the local crustal model at the centroid location; to use mode summation for the same calculation would require the recalculation of mode catalogues every time we encountered a new crustal structure.

Instead, we follow O'Toole & Woodhouse (2011) and compute accurate GPS waveforms for a plane layered elastic medium using the minor vector theory of Woodhouse (1980). This approach

Table 1. Crustal model used for the computations shown in Figs. 1 and 2, and in the inversion of GPS waveforms for the 2005 Fukuoka earthquake described in Section 4.1. This earth model was used by Kobayashi *et al.* (2006) in their finite fault inversions of HRGPS data for this event.

Thickness (km)	v_p (km s ⁻¹)	v_s (km s ⁻¹)	ρ (kg m ⁻³)
0.10	3.20	2.00	2.10
1.90	5.15	2.85	2.50
3.00	5.50	3.20	2.60
13.00	6.00	3.46	2.70
14.00	6.70	3.87	2.80
∞	7.70	4.30	3.30

ensures numerical stability at all frequencies, including 0 Hz, as is required if we wish to recover the static displacement as part of the synthetic time-series. Furthermore, the method can be straightforwardly adapted to enable the efficient computation of excitation and location kernels appropriate to GPS data, as shown in the Appendix.

The excitation kernels, being the partial derivatives of a synthetic seismogram with respect to the elements of the moment tensor, are simply the displacements arising from six elementary sources corresponding to each component of the moment tensor. Fig. 1 shows an example set of excitation kernels computed for a GPS receiver at a distance of 39.6 km and azimuth of 118.2° for a source with a depth of 35 km. The earth model used in the computation of these kernels is given in Table 1. The relatively small amplitudes of the M_{rr} , $M_{\theta\theta}$ and $M_{\phi\phi}$ kernels indicate that this location is not

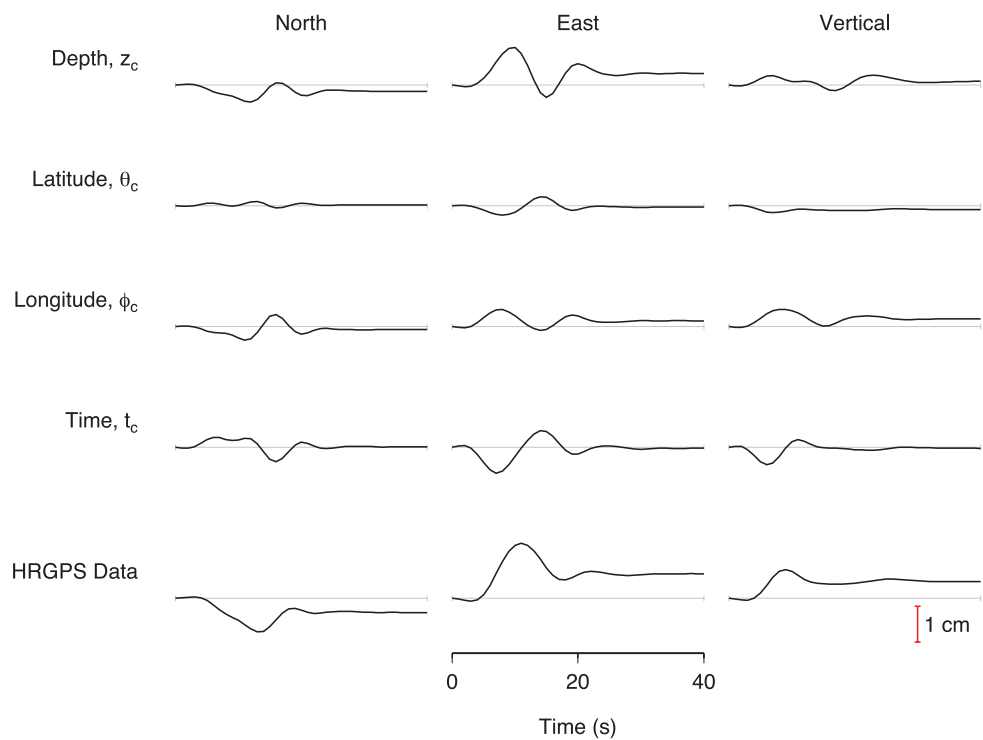


Figure 2. An example set of GPS location kernels computed for the same station and earth model as in Fig. 1, scaled to represent the change in seismogram caused by a 10 km shift of the source in each spatial coordinate and a 2 s perturbation of the origin time. The diversity of waveforms suggest that this location is sensitive to changes in the centroid’s position in space and time. These kernels also depend on the moment tensor, which is given in Table 2 (‘Iteration 0’ column); synthetic HRGPS data corresponding to this source are also shown for comparison purposes. All traces are plotted using the same vertical scale, indicated by the scale bar.

very sensitive to explosive sources. Furthermore, it is clear that these moment tensor components do not generate significant static displacements, and so if any coseismic offset were observed at this station it would require the excitation of the off-diagonal elements of the moment tensor.

Example location kernels are shown in Fig. 2; these were calculated using the same crustal model and source–receiver geometry as in Fig. 1. These kernels are scaled so that the $\partial_{\theta_c} u_k$, $\partial_{\phi_c} u_k$ and $\partial_{z_c} u_k$ kernels represent the change in the seismogram with respect

to a 10 km perturbation in each hypocentral coordinate; similarly the time kernel, $\partial_{t_c} u_k$, corresponds to a 2 s shift in origin time. Here, the variety of waveforms suggests that high-rate GPS data should allow us to resolve the location of the centroid in space and time, as we require. The shape of these kernels depends on the moment tensor, which is given in Table 2 (‘Iteration 0’ column); the synthetic HRGPS time-series corresponding to this source and station are also shown in Fig. 2 for comparison to the location kernels.

Table 2. The results of a numerical test of the CMT method using synthetic GPS waveforms. Synthetic data were computed for a strike-slip earthquake superimposed on an explosion (‘Input’ column); the initial location is 15 km away from the actual centroid. The CMT algorithm converges to the true source parameters after five iterations of the non-linear inversion scheme described in Section 2.2. The origin time is expressed relative to some reference value such as the hypocentral time determined from body wave arrivals; here the centroid of moment release occurred two seconds after this time. The moment tensors are given in units of 10^{19} Nm.

	Input	0	1	2	Iteration 3	4	5
Location:							
origin time (s)	2.00	0.00	1.80	2.45	1.88	2.01	1.99
latitude	34.00°N	33.90°N	33.90°N	34.02°N	33.99°N	34.00°N	34.00°N
longitude	130.00°E	130.10°E	130.07°E	129.98°E	130.01°E	130.00°E	130.00°E
depth (km)	35.00	30.00	31.76	32.05	35.86	34.99	35.00
Moment tensor:							
M_{rr}	1.0000	0.3406	0.4638	0.5376	1.0565	0.9938	1.0000
$M_{\theta\theta}$	1.0000	0.7798	0.8958	0.8990	1.0398	0.9991	0.9999
$M_{\phi\phi}$	1.0000	0.6349	0.7844	0.9232	1.0310	0.9994	1.0001
$M_{r\theta}$	0.0000	0.0005	−0.0281	0.0040	0.0143	0.0013	0.0000
$M_{r\phi}$	0.0000	0.1610	0.1638	0.1457	0.0102	0.0006	0.0000
$M_{\theta\phi}$	1.0000	0.1430	0.1736	0.5333	0.9308	0.9983	1.0000
Relative RMS		0.6023	0.4336	0.1463	0.0105	0.0000	0.0000

3 A TEST OF THE CMT METHOD USING SYNTHETIC GPS WAVEFORMS

To validate our implementation of GPS data in the CMT algorithm, we performed an inversion of a synthetic 1 Hz GPS waveform data set. We computed three component GPS seismograms for the point source given in Table 2 ('Input' column), which represents the superposition of a strike-slip earthquake with an explosion. Synthetics were calculated using an appropriate local crustal model as described in Table 1. For this experiment, we used a realistic distribution of stations, shown in Fig. 3, which corresponds to GPS receivers that observed the 2005 Fukuoka earthquake; we invert the actual GPS data for this earthquake in Section 4.1. Since we are interested in characterizing seismic sources at low frequencies, we

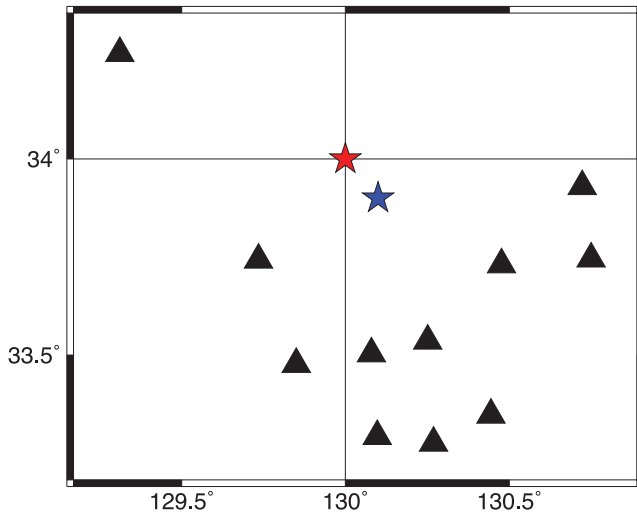


Figure 3. A realistic distribution of GPS receivers (black triangles) used in the inversions of synthetic GPS data shown in Tables 2 and 3. Here, the initial source location (blue star) is 15 km away from the true source (red star). This station distribution corresponds to that of the 2005 Fukuoka earthquake; we present an analysis of the actual HRGPS data for this earthquake in Section 4.1.

Table 3. As for Table 2 except that the synthetic HRGPS data set was calculated for a M_w 6.6 earthquake occurring on a fault with strike 30° , dip 80° and rake 20° , and only horizontal component waveforms were used in the inversion. We also impose the constraint that the trace of the moment tensor is zero, i.e. $M_{rr} + M_{\theta\theta} + M_{\phi\phi} = 0$. The beachballs output after each inversion iteration are also shown, and suggest that an error in the source location introduces a spurious non-double-couple component into the solution.

	Input	0	1	2	3	4	5	6
Location:								
origin time (s)	2.00	0.00	1.35	3.04	3.41	2.06	2.00	2.00
latitude	34.00°N	33.90°N	33.84°N	33.87°N	33.95°N	33.99°N	34.00°N	34.00°N
longitude	130.00°E	130.10°E	130.14°E	130.09°E	129.95°E	130.00°E	130.00°E	130.00°E
depth (km)	35.00	30.00	38.64	37.41	35.35	35.09	35.03	35.01
Moment tensor:								
M_{rr}	0.1170	-0.0389	-0.0693	-0.0357	0.1369	0.1322	0.1174	0.1171
$M_{\theta\theta}$	-0.8310	-0.2069	-0.3207	-0.3242	-0.5655	-0.7777	-0.8310	-0.8311
$M_{\phi\phi}$	0.7140	0.2458	0.3900	0.3599	0.4286	0.6455	0.7136	0.7140
$M_{r\theta}$	0.0194	-0.0926	-0.0937	-0.1602	-0.1750	-0.0178	0.0197	0.0194
$M_{r\phi}$	0.3600	0.0578	0.0455	0.0621	0.1848	0.2719	0.3581	0.3600
$M_{\theta\phi}$	-0.5130	-0.0616	-0.0807	-0.1073	-0.4616	-0.4206	-0.5131	-0.5129
Relative RMS		0.7421	0.6625	0.3941	0.2168	0.0112	0.0000	0.0000

applied a cosine low-pass filter with corner frequencies at 0.05 and 0.2 Hz to the synthetic data set and derivative kernels. The starting coordinates for the inversion are 15 km away from those of the true source, and the initial origin time is 2 s earlier than the correct value. We inverted this data set using the method set out in Section 2.2; ideally we should recover the source parameters used to calculate the synthetic data.

Table 2 shows the results of this synthetic test at each inversion iteration. The initial mislocation of the source means that the zeroth iteration produces a moment tensor that is far removed from the actual solution. Subsequently, the centroid moves towards its true position, resulting in incremental improvements in the values of the moment tensor. There is some trade-off between the origin time and depth, hence these parameters overshoot their true values during the second and third iterations, respectively. We recover the correct source parameters after five iterations of the inversion algorithm; this number is broadly comparable to our experience with inversions of teleseismic data. The success of this experiment demonstrates that our implementation of GPS data into the CMT algorithm is sound as it gives self-consistent results.

Since GPS measurement errors are typically largest in the vertical coordinate, in reality we may wish to ignore these data and invert just the horizontal component waveforms. To simulate one such situation, we performed a second synthetic inversion using horizontal displacements only. The setup of this experiment is much the same as before, except that synthetic HRGPS waveforms were computed for a M_w 6.6 earthquake occurring on a fault with strike 30° , dip 80° and rake 20° . In CMT inversions of real earthquake data it is generally assumed that there is no volume change associated with the seismic event, and so we also impose the additional constraint that the trace of the moment tensor is zero in this synthetic test. The results of this experiment are shown in Table 3, and indicate that the inversion algorithm performs well even in the absence of any vertical displacement data being available.

The 'radius of convergence' of the algorithm depends on the local form of the misfit function; in other synthetic experiments carried out under ideal conditions we were able to recover the true source parameters even when the initial location was in error by as much as 70 km and 25 s. In fact, for both of the earthquakes we examine later

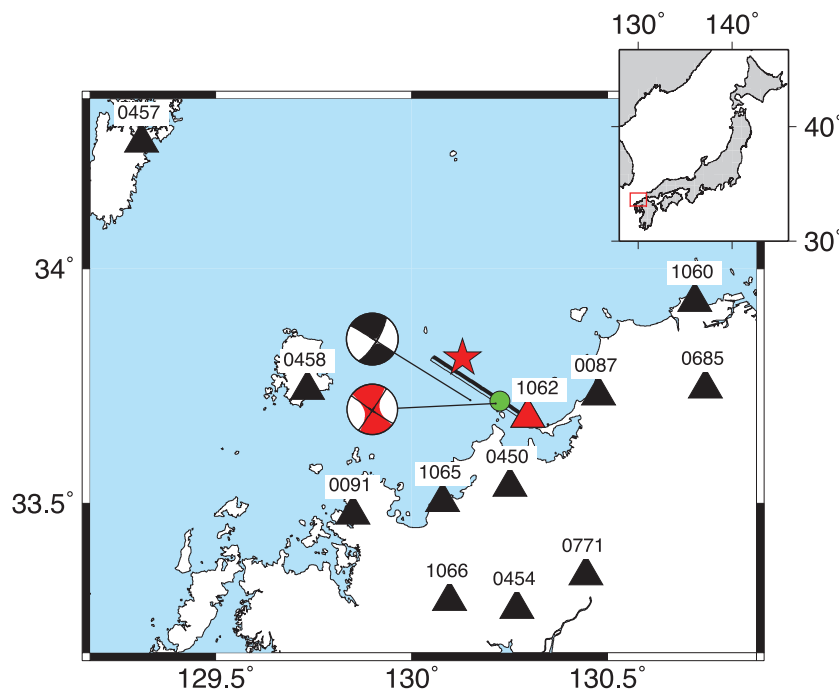


Figure 4. The distribution of GEONET GPS receivers (black triangles) used in our inversion of GPS waveforms from the 2005 M_w 6.6 Fukuoka earthquake. Our CMT solution is shown by the red beachball. The red star denotes the PDE catalogue hypocentre, which we use as the starting location for our inversion. For comparison, the Global CMT solution (black beachball) is also shown. The rectangle denotes the near-vertical fault plane assumed by Kobayashi *et al.* (2006); the top edge of their fault is indicated by the bold line. The centroid inferred from their inversion of three component data from the same 11 GPS stations is shown by the green circle. Our CMT solution is essentially collocated with the centroid of Kobayashi *et al.* (2006), and our best double-couple mechanism also compares favourably with the orientation of their fault plane (see Table 5). Data from station 1062 (red triangle) were not used in either inversion.

in this study, the USGS Preliminary Determination of Epicenters (PDE) hypocentre, which we assume for the zeroth iteration, is close enough to the centroid for our inversions of GPS data to converge.

Non-linearities encountered when a station lies in-between the inversion's starting location and the true centroid position may cause the inversion to become unstable. In practice this problem can be avoided by ignoring all stations within a certain distance of the initial epicentre. This approach obviously decreases the quantity of data available for inversion, however the loss of data is acceptable since it actually helps reduce the risk of the data set being contaminated by finite source effects. For the earthquakes we examine in Section 4—both of which have $M_w < 7.0$ —we find a threshold distance of 25 km is enough to prevent instabilities and finite source effects hampering the inversion.

4 CMT INVERSIONS USING HRGPS WAVEFORMS

As a proof of concept, we now attempt to perform CMT inversions using real 1 Hz GPS data obtained by Japan's GEONET for two recent events: the 2005 M_w 6.6 Fukuoka earthquake, and the 2008 M_w 6.9 Iwate–Miyagi earthquake. Rupture histories for these events have already been determined using these GPS waveforms by Kobayashi *et al.* (2006) and Yokota *et al.* (2009), respectively; interested readers should refer to these papers for details of the GPS processing methodologies employed. The performance of our inversion scheme can be assessed by comparing our CMT solutions to the first-order features of the finite fault slip models determined in these earlier studies, although one should bear in mind the differences in the inversion approaches which will be reflected in the results.

4.1 The 2005 M_w 6.6 Fukuoka, Japan earthquake

Fig. 4 shows the distribution of GEONET stations (triangles) that recorded 1 Hz GPS displacement waveforms for the 2005 March 20, M_w 6.6 Fukuoka earthquake. Kobayashi *et al.* (2006) inverted these data to infer the source process of this event, assuming that the earthquake occurred on a near-vertical fault (Fig. 4, rectangle), with a left-lateral strike-slip mechanism. They recovered a simple rupture history characterized by a single slip patch. Consequently, this event provides a good test of the CMT method applied to GPS data since we should recover a centroid location and mechanism close to that obtained by Kobayashi *et al.* (2006).

Apart from the obvious difference between our source parameterization and that employed by Kobayashi *et al.* (2006), we aim to emulate their inversion as closely as possible; we use their crustal structure, shown in Table 1, and extract identical minute-long windows from each displacement seismogram. One important difference is that we invert horizontal displacements only, as the vertical channels appear to be dominated by noise. Also, to mitigate against finite source effects contaminating the data set, we omit station 1062 (Fig. 4, red triangle) from our inversion as it lies within 25 km of the PDE hypocentre. Kobayashi *et al.* (2006) present an inversion that also ignores this station; in the following, any comparisons that we make relate to this particular solution.

As with our synthetic test, we apply a cosine low-pass filter to the data and synthetics, with corner frequencies at 0.05 and 0.2 Hz. Following the Global CMT algorithm, we constrain the trace of the moment tensor to be zero (i.e. $M_{rr} + M_{\theta\theta} + M_{\phi\phi} = 0$), so that there is no explosive component to the source. We take the starting location for the inversion from the PDE catalogue (Fig. 4, red star).




Table 4. The results of our CMT inversion of GPS waveforms recorded for the 2005 M_w 6.6 Fukuoka earthquake. The moment tensor is given in units of 10^{19} Nm.

	Initial	Final
Location:		
origin time (UT)	01 : 53 : 41.80	01 : 53 : 48.04
latitude	33.81°N	33.71°N
longitude	130.13°E	130.21°E
depth (km)	10.00	6.82
Moment tensor:		
M_{rr}		0.1365
$M_{\theta\theta}$		0.4420
$M_{\phi\phi}$		−0.5785
$M_{r\theta}$		0.0161
$M_{r\phi}$		0.0151
$M_{\theta\phi}$		0.2097
Relative RMS		0.0895

The result of our CMT inversion is given in Table 4, and shown as the red beachball in Fig. 4. Our moment tensor resembles the Global CMT mechanism (Fig. 4, black beachball), and is positioned about 7 km east of the catalogue solution, which is reasonable given the expected errors in Global CMT locations that arise from unmodelled 3-D earth structure (e.g. Valentine & Woodhouse 2010). Our centroid, located at 130.21° E, 33.71° N with depth 6.82 km, is consistent with the slip patch obtained by Kobayashi *et al.* (2006) from the same HRGPS data, which has approximate centroid coordinates of 130.23° E, 33.72° N and a depth of 6 km (Fig. 4, green circle). Since Kobayashi *et al.* (2006) assumed that the earthquake occurred purely as slip on a plane, it is instructive to compare our best double-couple solution to the orientation of their assumed fault. As Table 5 shows, our best double-couple solution corresponds to a fault mechanism that is almost identical to the one adopted by Kobayashi *et al.* (2006), and also compares favourably to the Global CMT best double-couple solution. Thus the mechanism and location that we recover appear to be consistent with those previously determined for this earthquake.

The non-double-couple component of a moment tensor can be expressed by the parameter $\epsilon = \lambda_{\min}/\lambda_{\max}$ where λ_{\min} and λ_{\max} are respectively the smallest and largest absolute values of the moment tensor's eigenvalues, with $\epsilon = 0$ corresponding to a pure double-couple. Values of ϵ for each solution are also given in Table 5. These ϵ values indicate that the Global CMT solution is almost pure double-couple whereas our CMT solution from HRGPS waveforms has a significant non-double-couple component, as is also apparent from a visual comparison of the beachballs plotted in Fig. 4. This

Table 5. A comparison of double-couple mechanisms for the 2005 M_w 6.6 Fukuoka earthquake. Our solution is very similar to the fault plane assumed in the finite fault inversion of Kobayashi *et al.* (2006) and the best double-couple mechanism from the Global CMT catalogue. The parameter ϵ , defined in Section 4.1, describes the deviation of the solution from a pure double-couple, which has $\epsilon = 0$.

	Strike (°)	Dip (°)	Rake (°)	Moment ($\times 10^{19}$ Nm)	ϵ	Best Double- Couple
This study	124	87	+2	0.55	0.22	
Kobayashi <i>et al.</i> (2006)	123	88	−1	0.88	0.00	
Global CMT catalogue	302	88	−14	0.92	0.02	

difference likely arises due to unmodelled complexities in source and structure, which will more strongly affect the near-field data. Regardless of the similarity of our result to earlier solutions, the excellent agreement between the observed GPS waveforms and those calculated for our final source, as shown in Fig. 5, suggests that it is possible to recover a reliable CMT solution from GPS waveform data.

4.2 2008 M_w 6.9 Iwate–Miyagi, Japan earthquake

To further validate the CMT method as applied to HRGPS data, we inverted a second set of 1 Hz GPS waveforms that were obtained for the 2008 June 13 M_w 6.9 Iwate–Miyagi earthquake. Fig. 6 shows the distribution of GEONET GPS receivers (triangles) that recorded this event. Yokota *et al.* (2009) inverted these data to infer the source process of this event, assuming a westward dipping thrust fault (Fig. 6, rectangle); they found that the rupture was best described by a single main slip patch with approximate centroid coordinates 140.88° E, 38.96° N and a depth of 3.6 km. The first-order features of this solution provide a useful check on the reasonableness of our CMT solution derived from the same GPS data set. However it should be kept in mind that, apart from the obvious differences in our source parameterizations, Yokota *et al.* (2009) used station-specific crustal models which we have not implemented, and—since three stations lie within 25 km of the hypocentre—we invert only a subset of the data that they used. We use the same filter parameters as before, and again invert only the horizontal GPS waveforms as the vertical displacements appear to be dominated by noise. The kernel functions are computed in the local earth model taken from Crust 2.0 (<http://igppweb.ucsd.edu/~gabi/rem.html>).

The result of our CMT inversion is given in Table 6, and shown as the red beachball in Fig. 6. Our centroid and moment tensor are similar to the Global CMT solution (Fig. 6, black beachball). Furthermore, our centroid is located close to that inferred from the slip distribution of Yokota *et al.* (2009, Fig. 6 green circle); the level of agreement between these locations is reasonable given the differences in earth models used. As Table 7 shows, our best double-couple mechanism is almost identical to the fault plane that Yokota *et al.* (2009) used, and also compares well to the best double-couple solution from the Global CMT catalogue. The ϵ values corresponding to these different results, also shown in Table 7, indicate that both our CMT solution and the Global CMT solution have a non-double-couple component, although the deviation from a pure double-couple is larger for our near-field solution. So the CMT solution that we obtain from GPS data for this earthquake is consistent with independently determined mechanisms and locations. Furthermore the excellent agreement between the observed and synthetic GPS waveforms, as Fig. 7 shows, demonstrates that our CMT solution explains the data very well and implies that—at low frequencies—a point moment tensor source is a sufficient model for this earthquake.

5 DISCUSSION

Our inversions of synthetic and real GPS waveforms clearly demonstrate the potential value of HRGPS data for determining the first-order source parameters of an earthquake. The good agreement between our CMT solutions and other independent source models strongly suggests that the data selection, processing and inversion schemes described in this paper are robust. For both of the earthquakes that we have analysed our CMT solution explains the GPS data very well, with a variance reduction of over 90 per cent.

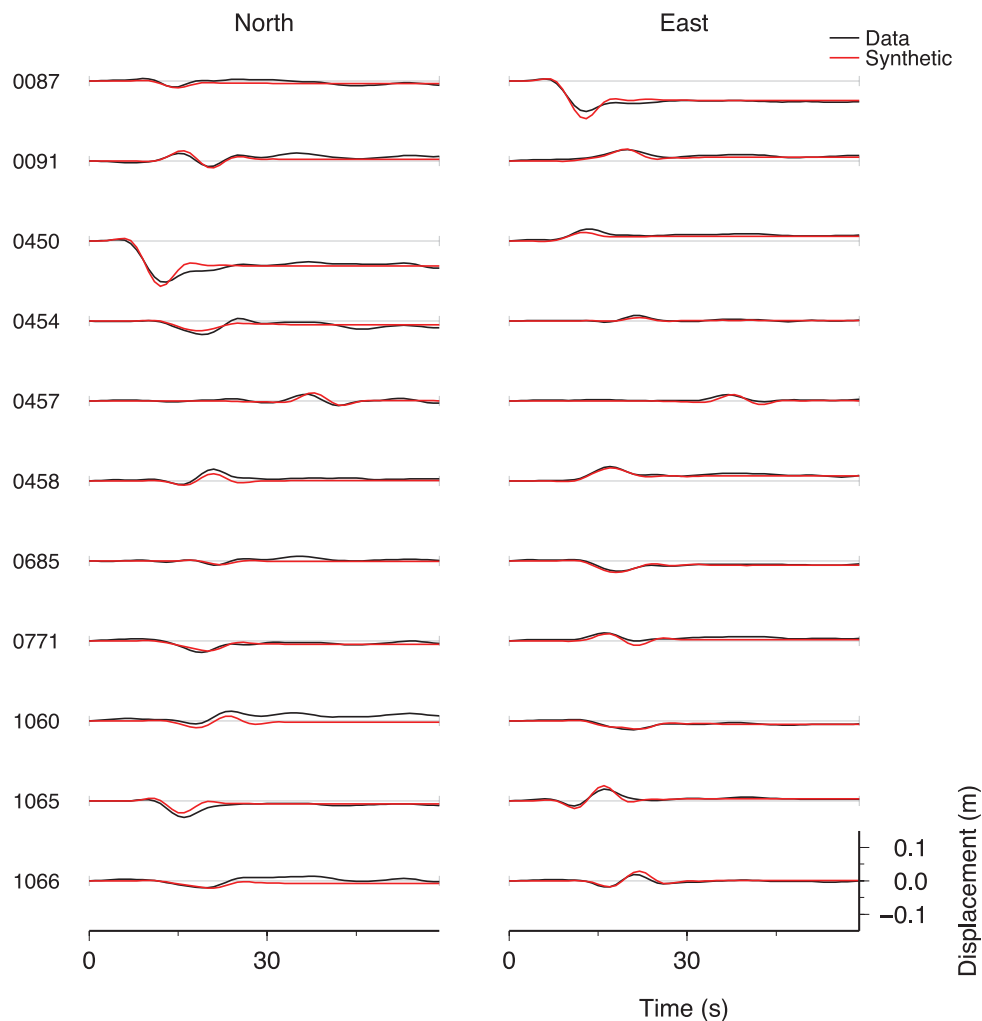


Figure 5. GPS waveforms (black traces) observed at the stations shown in Fig. 4 after the 2005 M_w 6.6 Fukuoka earthquake, and used in our CMT inversion. Synthetic seismograms (red traces) computed for our recovered CMT solution fit the data well in both phase and amplitude, with an overall variance reduction of 91 per cent. Time is relative to the PDE hypocentral time.

This level of agreement suggests that a point moment tensor source is a good model for these moderate magnitude earthquakes, even for near-field data.

Although we have only analysed two events, some features of these preliminary results are worthy of further discussion. For both earthquakes, we find that the origin time perturbation is positive, that is, the centroid time is later than the hypocentral time, which is expected for a rupture of finite duration and follows from the definition of the centroid as opposed to the hypocentre. The larger earthquake required a greater shift in origin time, which is consistent with the observation that, for simple ruptures, the time perturbation is analogous to the earthquake's half-duration (Dziewonski & Woodhouse 1983a).

Both of the HRGPS CMT solutions that we have determined have non-double-couple components that are larger than those in the corresponding Global CMT solutions. These could arise from source complexities such as curved or multiple faults, and unmodelled 3-D structural effects that impact the near-field data more heavily than the longer-period teleseismic waveforms used to construct Global CMT solutions.

We also find that both of our data inversions yield lower moment estimates than the Global CMT solutions. Some of this disagree-

ment can be explained by the shallow centroid depths that we recover relative to the catalogue solutions, which are fixed to a depth of 12 km during the inversion. Since our focal depths agree with those obtained from finite fault slip inversions we believe that the shallow depths we recover are real and can be trusted. It is interesting that we can obtain stable moment tensors for earthquakes as shallow as 3 km using GPS waveforms, given the well known problem of determining the $M_{r\theta}$ and $M_{r\phi}$ components of shallow events from long-period teleseismic data. High-rate GPS waveforms from more earthquakes obviously must be analysed to assess the general validity of this observation.

The scope of our analysis has so far been limited to only two events principally because seismologists' access to GPS waveforms is on a somewhat *ad hoc* basis. Melgar *et al.* (2011) estimate that since 2002 Japan's GEONET has recorded 1 Hz GPS data for 29 earthquakes larger than magnitude 7.0. As noted by Larson (2009) it is desirable for further HRGPS waveform data sets to be made publicly available in seismological repositories. With better access to data, it is possible that the method outlined in this paper could be applied systematically to determine earthquake source parameters from GPS waveforms. Such an undertaking may be useful for improving the completeness of seismic catalogues in the immediate

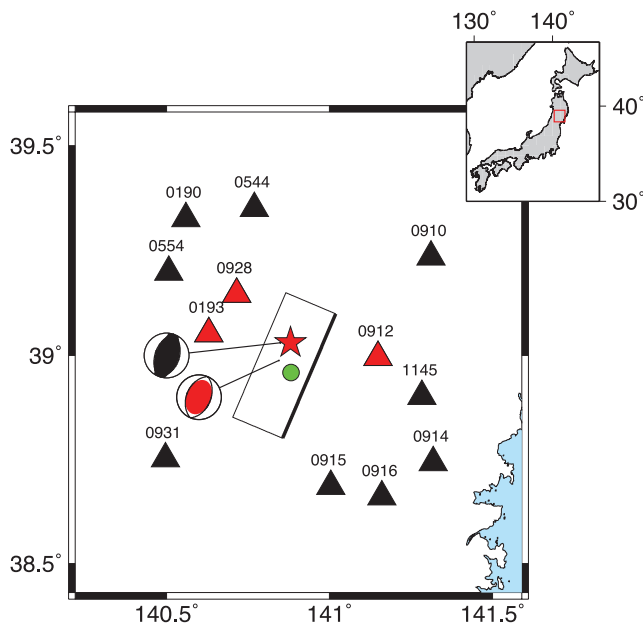


Figure 6. The distribution of GEONET GPS receivers (black triangles) used in our inversion of GPS waveforms from the 2008 M_w 6.9 Iwate–Miyagi earthquake. Our CMT solution is shown by the red beachball. We did not invert data from stations 0928, 0193 and 0912 (red triangles) because of their proximity to the PDE catalogue hypocentre (red star) which we use as the starting location for our inversion. For comparison, the Global CMT solution (black beachball) is also shown. The rectangle denotes the westward dipping thrust fault assumed by Yokota *et al.* (2009); the top edge of their fault is indicated by the bold line. The centroid inferred from their inversion of three component data from all of the above stations is shown by the green circle. Our best double-couple mechanism compares favourably with the orientation of their fault plane (see Table 7).

Table 6. The results of our CMT inversion of GPS waveforms recorded for the 2008 M_w 6.9 Iwate–Miyagi earthquake. The moment tensor is given in units of 10^{19} Nm.

	Starting	Final
Location:		
origin time (UT)	23 : 43 : 45.40	23 : 43 : 52.37
latitude	39.03°N	38.99°N
longitude	140.88°E	140.84°E
depth (km)	7.80	3.24
Moment tensor:		
M_{rr}		2.5372
$M_{\theta\theta}$		−0.6496
$M_{\phi\phi}$		−1.8876
$M_{r\theta}$		0.0270
$M_{r\phi}$		0.1362
$M_{\theta\phi}$		−0.6299
Relative RMS		0.0815

aftermath of great earthquakes, when teleseismic data may be unusable due to the interference of waves generated by closely spaced aftershocks. Since we use only a short window of data, and a small number of near-field stations, it may be possible to avoid any such interference by using HRGPS data. Dynamic displacements have been observed using modern GPS networks for earthquakes that are as small as M_w 6.3; this magnitude represents a lower bound on the size of events which could be studied using the HRGPS waveform inversion algorithm we have developed.

Table 7. A comparison of double-couple mechanisms for the 2008 M_w 6.9 Iwate–Miyagi earthquake. Our solution is very similar to the fault plane assumed in the finite fault inversion of Yokota *et al.* (2009) and the best double-couple mechanism from the Global CMT catalogue. The parameter ϵ , defined in Section 4.1, describes the deviation of the solution from a pure double-couple, which has $\epsilon = 0$.

	Strike (°)	Dip (°)	Rake (°)	Moment ($\times 10^{19}$ Nm)	ϵ	Best Double-Couple
This study	203	43	+91	2.3	0.15	
Yokota <i>et al.</i> (2009)	203	37	+90	2.7	0.00	
Global CMT catalogue	201	48	+92	2.6	0.07	

To fully exploit the available GPS data resource, we need to validate our method for larger earthquakes. Thus far we have assumed that the source acts instantaneously, which is only reasonable if the data is long-period relative to the duration of the earthquake. For larger events, in addition to filtering the data at lower frequencies, we will need to implement a source time function of realistic duration. As the spatial dimensions of the source grow, our strategy to minimize finite fault effects—excluding data from stations that are less than 25 km away from the source—will also need to be refined. Neither of these implementation issues fundamentally prohibits CMT inversions of HRGPS waveforms from larger earthquakes, and existing scaling laws (e.g. Kanamori & Anderson 1975) suggest that simple rules can be applied to accommodate the finite spatial and temporal extent of the earthquake source.

There is growing interest in using GPS data to rapidly characterize seismic sources for the purpose of earthquake early warning (e.g. Crowell *et al.* 2009). The inversion method described in this paper could be used to determine the location, mechanism and moment of earthquakes from HRGPS waveforms in real time. So far, rapid source inversions of GPS data streams have exploited only the static displacement field (Allen & Ziv 2011; Melgar *et al.* 2011); additional information about the source could be gained by including frequencies other than 0 Hz in the inversion. Furthermore, the CMT algorithm is amenable to real-time implementation since the data can be windowed automatically and the only *a priori* information needed is a starting source location, such as the hypocentre determined from P -wave arrival times, and an earth model, which—in the absence of a more appropriate local alternative—can be found from Crust 2.0. The rate determining step in the inversion is the time taken to compute the derivative kernels. Using 18 processors, typical inversion times for data sets of the size presented in this report are of the order 5 min; this time can doubtless be significantly decreased using large, state of the art cluster supercomputers.

6 CONCLUSION

In this paper, we have developed a method for retrieving the best point source parameters of an earthquake from displacement seismograms measured using GPS receivers. While we have focused on the application of GPS time-series to studies of the seismic source at low frequencies, the generality of this method should enable us to use additional long-period near-field data—perhaps provided by accelerometers—in future CMT inversions. Our approach is based on the waveform inversion algorithm described by Dziewonski *et al.* (1981), which has been widely applied to long-period teleseismic data.

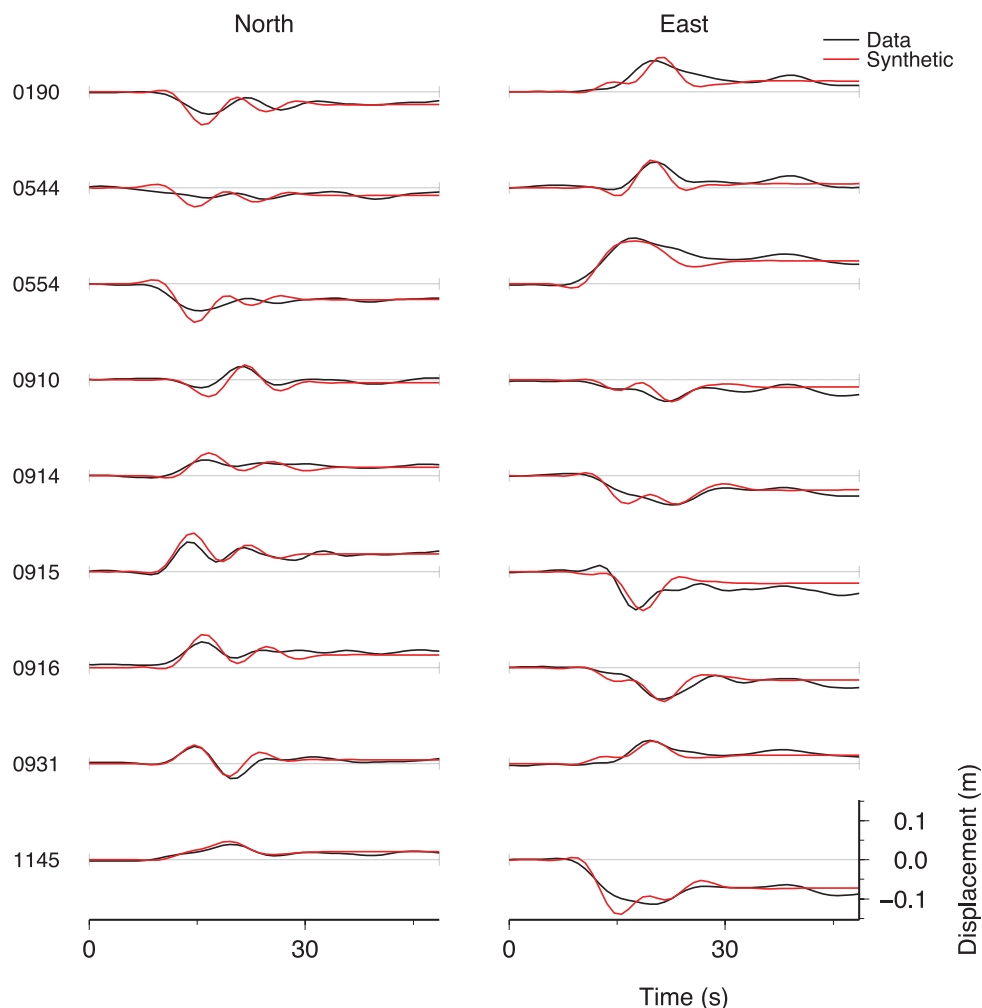


Figure 7. GPS waveforms (black traces) observed at the stations shown in Fig. 6 after the M_w 6.9 Iwate–Miyagi earthquake, and used in our CMT inversion. Synthetic seismograms (red traces) computed for our recovered CMT solution fit the data well in both phase and amplitude, with an overall variance reduction of 91 per cent. Time is relative to the PDE hypocentral time.

Using this method, we have inverted 1 Hz GPS data sets pertaining to two recent earthquakes in Japan. The CMT solutions that we recover are consistent with finite source models determined from the same GPS data sets, and also with the Global CMT catalogue solutions obtained from long-period teleseismic waveform data. This agreement suggests that we can recover reliable source parameters from GPS data. Our CMT solutions explain the GPS data very well, implying that a point moment tensor source is a good model for these earthquakes even in the seismic near-field. There is much scope for further development of the method presented in this study, particularly in the context of earthquakes larger than magnitude 7.0. By providing a framework for the inversion of HRGPS waveforms that mirrors the one used for CMT inversions of teleseismic data, the present work should allow direct comparison and amalgamation of information from diverse data sets, yielding an improved understanding of earthquake source models and their uncertainties.

ACKNOWLEDGMENTS

We are grateful to Reiji Kobayashi and Yusuke Yokota for supplying the 1 Hz GPS data sets used in this report. We also thank two anonymous reviewers for their comments which helped improve the original manuscript. In addition, TBO'T thanks David Al-Attar for many

helpful discussions. TBO'T is supported by the UK Natural Environment Research Council under the grant NE/H527791/1; APV is supported by QUEST, an Initial Training Network funded under the 'Marie Curie Actions' of the European Commission (grant 238007). Computational facilities are supported under grant NE/B505997/1.

REFERENCES

- Al-Attar, D. & Woodhouse, J.H., 2008. Calculation of seismic displacement fields in self-gravitating earth models—applications of minors vectors and symplectic structure, *Geophys. J. Int.*, **175**, 1176–1208, doi:10.1111/j.1365-246X.2008.03961.x.
- Allen, R.M. & Ziv, A., 2011. Application of real-time GPS to earthquake early warning, *Geophys. Res. Lett.*, **38**, L16310, doi:10.1029/2011GL047947.
- Ammon, C.J., Lay, T., Kanamori, H. & Cleveland, M., 2011. A rupture model of the great 2011 Tohoku earthquake, *Earth, Planets and Space*, **20**, 1–4.
- Avallone, A. *et al.*, 2011. Very high rate (10 Hz) GPS seismology for moderate-magnitude earthquakes: the case of the M_w 6.3 L'Aquila (central Italy) event, *J. geophys. Res.*, **116**, B02305, doi:10.1029/2010JB007834.
- Bock, Y., Prawirodirdjo, L. & Melbourne, T.I., 2004. Detection of arbitrarily large dynamic ground motions with a dense high-rate GPS network, *Geophys. Res. Lett.*, **31**, L06604, doi:10.1029/2003GL019150.

- Bock, Y., Melgar, D. & Crowell, B.W., 2011. Real-time strong-motion broadband displacements from collocated GPS and accelerometers, *Bull. seism. Soc. Am.*, **101**(6), 2904–2925, doi:10.1785/012011007.
- Crowell, B.W., Bock, Y. & B., S.M., 2009. Demonstration of earthquake early warning using total displacement waveforms from real-time GPS networks, *Seism. Res. Lett.*, **80**(5), 772–782.
- Davis, J.P. & Smalley, R., 2009. Love wave dispersion in central North America determined using absolute displacement seismograms from high-rate GPS, *J. geophys. Res.*, **114**, B11303, doi:10.1029/2009JB006288.
- Delouis, B., Nocquet, J.-M. & Vallée, M., 2010. Slip distribution of the February 27, 2010 Mw = 8.8 Maule Earthquake, central Chile, from static and high-rate GPS, InSAR, and broadband teleseismic data, *Geophys. Res. Lett.*, **37**, L17305, doi:10.1029/2010GL043899.
- Dziewonski, A.M. & Woodhouse, J.H., 1983a. An experiment in systematic study of global seismicity: centroid-moment tensor solutions for 201 moderate and large earthquakes of 1981, *J. geophys. Res.*, **88**(B4), 3247–3271.
- Dziewonski, A.M. & Woodhouse, J.H., 1983b. Studies of the seismic source using normal-mode theory, in *Earthquakes: Observation, Theory and Interpretation*, Proceedings of the International School of Physics “Enrico Fermi”, Course LXXXV, Amsterdam, pp. 45–137.
- Dziewonski, A.M., Friedman, A., Giardini, D. & Woodhouse, J.H., 1983. Global seismicity of 1982: centroid-moment tensor solutions for 308 earthquakes, *Phys. Earth planet. Inter.*, **33**, 76–90.
- Dziewonski, A.M., Chou, T.-A. & Woodhouse, J.H., 1981. Determination of earthquake source parameters from waveform data for studies of global and regional seismicity, *J. geophys. Res.*, **86**(B4), 2825–2852.
- Gilbert, F. & Backus, G.E., 1966. Propagator matrices in elastic wave and vibration problems, *Geophysics*, **31**(2), 326–332.
- Gilbert, F. & Dziewonski, A.M., 1975. An application of normal mode theory to the retrieval of structural parameters and source mechanisms from seismic spectra, *Phil. Trans. R. Soc.*, **278**(1280), 187–269.
- Hammond, W.C., Brooks, B.A., Bürgmann, R., Heaton, T., Jackson, M., Lowry, A.R. & Anandakrishnan, S., 2010. *The Scientific Value of High-Rate, Low-Latency GPS Data*, White Paper, Earthscope Plate Boundary Observatory Advisory Committee, UNAVCO, Boulder, CO.
- Ji, C., Larson, K.M., Tan, Y., Hudnut, K.W. & Choi, K., 2004. Slip history of the 2003 San Simeon earthquake constrained by combining 1-Hz GPS, strong motion, and teleseismic data, *Geophys. Res. Lett.*, **31**, L17608, doi:10.1029/2004GL020448.
- Kanamori, H. & Anderson, D., 1975. Theoretical basis of some empirical relations in seismology, *Bull. seism. Soc. Am.*, **65**(5), 1073–1095.
- Kobayashi, R., Miyazaki, S. & Koketsu, K., 2006. Source processes of the 2005 West Off Fukuoka Prefecture earthquake and its largest aftershock inferred from strong motion and 1-Hz GPS data, *Earth, Planets and Space*, **58**, 57–62.
- Kouba, J., 2003. Measuring seismic waves induced by large earthquakes with GPS, *Studia Geophysica et Geodaetica*, **47**, 741–755.
- Larson, K.M., 2009. GPS seismology, *J. Geod.*, **83**, 227–233.
- Larson, K.M., Bodin, P. & Gombert, J., 2003. Using 1-Hz GPS data to measure deformations caused by the Denali fault earthquake., *Science*, **300**, 1421–1424, doi:10.1126/science.1083780.
- Lay, T., 2011. Great earthquake ruptures in the age of seismo-geodesy, *Am. geophys. Un. Fall Meet.*, Abstract S23C-01.
- Melgar, D., Bock, Y. & Crowell, B.W., 2011. Real-time centroid moment tensor determination for large earthquakes from local and regional displacement records, *Geophys. J. Int.*, **188**, 703–718, doi:10.1111/j.1365-246X.2011.05297.x.
- Menke, W., 1989. *Geophysical Data Analysis: Discrete Inverse Theory*, Academic Press, New York, NY.
- Miyazaki, S. *et al.*, 2004. Modeling the rupture process of the 2003 September 25 Tokachi-Oki (Hokkaido) earthquake using 1-Hz GPS data, *Geophys. Res. Lett.*, **31**, L21603, doi:10.1029/2004GL021457.
- Nikolaidis, R.M., Bock, Y., de Jonge, P.J., Shearer, P., Agnew, D.C. & Van Domselaar, M., 2001. Seismic wave observations with the Global Positioning System, *J. geophys. Res.*, **106**(B10), doi:10.1029/2001JB000329.
- O’Toole, T.B. & Woodhouse, J.H., 2011. Numerically stable computation of complete synthetic seismograms including the static displacement in plane layered media, *Geophys. J. Int.*, **187**, 1516–1536, doi:10.1111/j.1365-246X.2011.05210.x.
- Pondrelli, S., Morelli, A., Ekström, G., Mazza, S., Boschi, E. & Dziewonski, A.M., 2002. European–Mediterranean regional centroid-moment tensors: 1997–2000, *Phys. Earth planet. Inter.*, **130**, 71–101.
- Riley, K., Hobson, M.P. & Bence, S.J., 2007. *Mathematical Methods for Physics and Engineering*, 3rd edn, Cambridge University Press, Cambridge.
- Shi, C., Lou, Y., Zhang, H., Zhao, Q., Geng, J., Wang, R., Fang, R. & Liu, J., 2010. Seismic deformation of the Mw 8.0 Wenchuan earthquake from high-rate GPS observations, *Adv. Space Res.*, **46**, 228–235, doi:10.1026/j.asr.2010.03.006.
- Valentine, A.P. & Woodhouse, J.H., 2010. Reducing errors in seismic tomography: combined inversion for sources and structure, *Geophys. J. Int.*, **180**, 847–857, doi:10.1111/j.1365-246X.2009.04452.x.
- Vigny, C. *et al.*, 2011. The 2010 Mw 8.8 Maule megathrust earthquake of Central Chile, monitored by GPS, *Science*, **332**(6036), 1417–1421, doi:10.1126/science.1204132.
- Woodhouse, J.H., 1980. Efficient and stable methods for performing seismic calculations in stratified media, in *Physics of the Earth’s Interior*, Proceedings of the International School of Physics “Enrico Fermi”, Course LXXVIII, North Holland, Amsterdam, pp. 127–151.
- Yang, H.-Y., Zhao, L. & Hung, S.-H., 2010. Synthetic seismograms by normal-mode summation: a new derivation and numerical examples, *Geophys. J. Int.*, **183**, 1613–1632, doi:10.1111/j.1365-246X.2010.04820.x.
- Yokota, Y., Koketsu, K., Hikima, K. & Miyazaki, S., 2009. Ability of 1-Hz GPS data to infer the source process of a medium-sized earthquake: the case of the 2008 Iwate-Miyagi Nairiku, Japan, earthquake, *Geophys. Res. Lett.*, **36**, L12301, doi:10.1029/2009GL037799.
- Yue, H. & Lay, T., 2011. Inversion of high-rate (1 sps) GPS data for rupture process of the 11 March 2011 Tohoku earthquake (Mw 9.1), *Geophys. Res. Lett.*, **38**, L00G09, doi:10.1029/2011GL048700.

APPENDIX: DIRECT CALCULATION OF ACCURATE LOCATION KERNELS

Here, we derive expressions for the location kernels which we use in our CMT inversions of GPS waveforms. We have verified our implementation of the theory presented here through comparisons to derivative kernels calculated using the method of finite differences. Following O’Toole & Woodhouse (2011), we begin by defining a right-handed Cartesian coordinate system (x, y, z) related to cylindrical polar coordinates (r, ϕ, z) by

$$x = x_1 = r \cos \phi, \quad (\text{A1})$$

$$y = x_2 = r \sin \phi, \quad (\text{A2})$$

$$z = x_3, \quad (\text{A3})$$

where the positive z -axis is directed upwards.

A1 Centroid time kernel

The centroid time kernel is the negative of the time derivative of the synthetic seismogram and is straightforward to calculate in the frequency domain via multiplication of the synthetic spectra by $-i\omega$.

A2 Epicentral location kernels

Consider a seismic source located at $\mathbf{x}_s = (x_s, y_s, z_s)$. We seek the derivative of the displacement field, $\mathbf{u}(r, \phi, t)$, with respect to the epicentral location. Using the chain rule, we can write

$$\frac{\partial \mathbf{u}}{\partial x_s} = \frac{\partial \mathbf{u}}{\partial r} \frac{\partial r}{\partial x_s} + \frac{\partial \mathbf{u}}{\partial \phi} \frac{\partial \phi}{\partial x_s} \quad (\text{A4})$$

$$\frac{\partial \mathbf{u}}{\partial y_s} = \frac{\partial \mathbf{u}}{\partial r} \frac{\partial r}{\partial y_s} + \frac{\partial \mathbf{u}}{\partial \phi} \frac{\partial \phi}{\partial y_s} \quad (\text{A5})$$

with

$$\frac{\partial r}{\partial x_s} = -\cos \phi, \quad \frac{\partial \phi}{\partial x_s} = \frac{\sin \phi}{r}, \quad (\text{A6})$$

$$\frac{\partial r}{\partial y_s} = -\sin \phi, \quad \frac{\partial \phi}{\partial y_s} = \frac{-\cos \phi}{r}. \quad (\text{A7})$$

From eqs (27)–(29) of O'Toole & Woodhouse (2011), we can write the displacement field as an integral over angular frequency ω and horizontal wavenumber k

$$u_r(r, \phi, t) = \int d\omega \frac{e^{i\omega t}}{2\pi i\omega} \sum_{m=-2}^2 e^{im\phi} K_r^m(r, \omega) \quad (\text{A8})$$

$$u_\phi(r, \phi, t) = \int d\omega \frac{e^{i\omega t}}{2\pi i\omega} \sum_{m=-2}^2 e^{im\phi} K_\phi^m(r, \omega) \quad (\text{A9})$$

$$u_z(r, \phi, t) = \int d\omega \frac{e^{i\omega t}}{2\pi i\omega} \sum_{m=-2}^2 e^{im\phi} K_z^m(r, \omega) \quad (\text{A10})$$

with

$$K_r^m(r, \omega) = \frac{1}{2\pi} \int_0^\infty [k V_m J'_m(kr) + imr^{-1} W_m J_m(kr)] dk \quad (\text{A11})$$

$$K_\phi^m(r, \omega) = \frac{1}{2\pi} \int_0^\infty [imr^{-1} V_m J_m(kr) - k W_m J'_m(kr)] dk \quad (\text{A12})$$

$$K_z^m(r, \omega) = \frac{1}{2\pi} \int_0^\infty k U_m J_m(kr) dk, \quad (\text{A13})$$

where $J_m(kr)$ is a Bessel function and a prime denotes differentiation with respect to its argument. U_m , V_m and W_m are the displacement elements of the stress-displacement vectors. Differentiating expressions (A8)–(A10) with respect to ϕ we obtain

$$\frac{\partial u_i}{\partial \phi} = \int d\omega \frac{e^{i\omega t}}{2\pi i\omega} \sum_m im e^{im\phi} K_i^m(r, \omega) \quad (\text{A14})$$

The derivatives of (A8)–(A10) with respect to the radial coordinate are of the form

$$\frac{\partial u_i}{\partial r} = \int d\omega \frac{e^{i\omega t}}{2\pi i\omega} \sum_{m=-2}^2 e^{im\phi} \frac{\partial K_i^m}{\partial r} \quad (\text{A15})$$

From (A11)–(A13) we write

$$\frac{\partial K_r^m}{\partial r} = \frac{1}{2\pi} \int_0^\infty \left[k V_m \frac{\partial}{\partial r} J'_m(kr) - \frac{im}{r^2} W_m J_m(kr) + \frac{im}{r} W_m k J'_m(kr) \right] dk \quad (\text{A16})$$

$$\frac{\partial K_\phi^m}{\partial r} = \frac{1}{2\pi} \int_0^\infty \left[-\frac{im}{r^2} V_m J_m(kr) + \frac{im}{r} V_m k J'_m(kr) - k W_m \frac{\partial}{\partial r} J'_m(kr) \right] dk \quad (\text{A17})$$

$$\frac{\partial K_z^m}{\partial r} = \frac{1}{2\pi} \int_0^\infty k^2 U_m J_m'(kr) dk. \quad (\text{A18})$$

To improve computational efficiency, we seek an expression for the second derivative of the Bessel function

$$\frac{\partial}{\partial r} J_m'(kr) = k J_m''(kr) \quad (\text{A19})$$

in terms of its lower derivatives, which we have already calculated. Rearranging Bessel's equation we obtain

$$\frac{\partial}{\partial r} J_m'(kr) = \frac{1}{kr^2} [-kr J_m'(kr) - (k^2 r^2 - m^2) J_m(kr)] \quad (\text{A20})$$

which we use in (A16)–(A18) to calculate the radial derivatives of the displacement.

A3 Source depth kernel

The algorithm of O'Toole & Woodhouse (2011) allows us to solve systems of inhomogeneous ordinary differential equations of the form

$$\frac{\partial \mathbf{b}}{\partial z} = \mathbf{A} \mathbf{b} + \mathbf{f}, \quad (\text{A21})$$

where the stress-displacement vector \mathbf{b} , the system matrix \mathbf{A} and the source representation \mathbf{f} are functions only of the vertical coordinate, z . Assuming that the source does not lie on a structural discontinuity, we can differentiate (A21) with respect to the source depth z_s to obtain

$$\frac{\partial}{\partial z} \frac{\partial \mathbf{b}}{\partial z_s} = \mathbf{A} \frac{\partial \mathbf{b}}{\partial z_s} + \frac{\partial \mathbf{f}}{\partial z_s}. \quad (\text{A22})$$

Since this expression is of the same form as (A21), we can use the same method of solution to obtain the source depth kernel by replacing the force term with its derivative with respect to source depth. The action of the source is implemented as a discontinuity in the solution at the source depth. After Al-Attar & Woodhouse (2008), who presented a similar result for the equivalent problem in a spherical geometry, we convert the force term into a slip condition at the source depth as follows.

A trial solution of (A21) is

$$\mathbf{b}(z) = \mathbf{P}(z, z_2) \mathbf{v}(z), \quad (\text{A23})$$

where $\mathbf{v}(z)$ is to be determined; $\mathbf{P}(z, z_2)$ is the propagator matrix (Gilbert & Backus 1966) satisfying

$$\frac{\partial}{\partial z} \mathbf{P}(z, z_2) = \mathbf{A}(z) \mathbf{P}(z, z_2), \quad \mathbf{P}(z_2, z_2) = \mathbf{1} \quad (\text{A24})$$

and $\mathbf{1}$ is the identity matrix. Differentiating (A23) with respect to z , we obtain

$$\frac{\partial}{\partial z} \mathbf{v}(z) = \mathbf{P}^{-1}(z, z_2) \mathbf{f}(z). \quad (\text{A25})$$

Integrating this expression upwards from some arbitrary depth z_2 below the source (i.e. $z_2 < z_s$) we find a particular integral of (A21) is

$$\mathbf{v}(z) = \int_{z_2}^z \mathbf{P}^{-1}(z', z_2) \mathbf{f}(z') dz' + \mathbf{v}(z_2) \quad (\text{A26})$$

and recalling the definition (A23) we can express the stress-displacement vector as

$$\mathbf{b}(z) = \int_{z_2}^z \mathbf{P}(z, z') \mathbf{f}(z') dz' + \mathbf{P}(z, z_2) \mathbf{v}(z_2), \quad (\text{A27})$$

where we have also used the property of the propagator matrix $\mathbf{P}(z_1, z_2) = \mathbf{P}^{-1}(z_2, z_1)$. Since the solution to the homogeneous equation is a continuous function of depth, the discontinuity at the source depth comes from the consideration of this particular integral alone. The force term is given by

$$\mathbf{f} = \mathbf{a} \delta(z - z_s) + \mathbf{c} \delta'(z - z_s), \quad (\text{A28})$$

where $\delta(z - z_s)$ is the Dirac delta function and the prime denotes its derivative. Using this expression in (A27), the solution above the source is

$$\mathbf{b}(z) = \mathbf{P}(z, z_s) \mathbf{a}(z_s) - \int_{z_2}^z \frac{\partial}{\partial z'} \mathbf{P}(z, z') \mathbf{c}(z') \delta(z' - z_s) dz' + \mathbf{P}(z, z_2) \mathbf{v}(z_2), \quad (\text{A29})$$

where we have used the result (Riley *et al.* 2007)

$$\int_I f(z) \delta^{(n)}(z) dz = (-1)^n \int_I f^{(n)}(z) \delta(z) dz \quad (\text{A30})$$

for the n th derivative of the Dirac delta function in the interval I . We obtain the derivative of the propagator matrix with respect to its second argument by considering

$$\frac{\partial}{\partial z'} (\mathbf{P}(z, z') \mathbf{P}^{-1}(z, z')) = \mathbf{0} \quad (\text{A31})$$

which leads to

$$\frac{\partial}{\partial z'} \mathbf{P}(z, z') = -\mathbf{P}(z, z') \mathbf{A}(z'). \quad (\text{A32})$$

Using this result in (A29), we can write the solution as

$$\mathbf{b}(z) = \begin{cases} \mathbf{P}(z, z_2) \mathbf{v}(z_2) & z \in [z_2, z_s) \\ \mathbf{P}(z, z_2) \mathbf{v}(z_2) + \mathbf{P}(z, z_s) \mathbf{a}(z_s) + \mathbf{P}(z, z_s) \mathbf{A}(z_s) \mathbf{c}(z_s) & z \in (z_s, z_1] \end{cases} \quad (\text{A33})$$

It follows that the point source (A28) produces a discontinuity, \mathbf{s} , in the solution vector at the source depth, given by

$$\mathbf{s} = \lim_{\epsilon \downarrow 0} [\mathbf{b}(z_s + \epsilon) - \mathbf{b}(z_s - \epsilon)] = \mathbf{a}(z_s) + \mathbf{A}(z_s) \mathbf{c}(z_s). \quad (\text{A34})$$

Applying the same argument to (A22), we find the derivative of the force term (A28) with respect to the source depth is

$$\frac{\partial \mathbf{f}}{\partial z_s} = -\mathbf{a}'(z - z_s) - \mathbf{c}\delta''(z - z_s) \quad (\text{A35})$$

which corresponds to a discontinuity in the solution vector at the source depth given by

$$\mathbf{s} = \lim_{\epsilon \downarrow 0} \left[\frac{\partial \mathbf{b}(z_s + \epsilon)}{\partial dz_s} - \frac{\partial \mathbf{b}(z_s - \epsilon)}{\partial dz_s} \right] = -\mathbf{A}(z_s) \mathbf{a}(z_s) - \mathbf{A}(z_s) \mathbf{A}(z_s) \mathbf{c}(z_s). \quad (\text{A36})$$

Thus we can easily calculate the derivative with respect to source depth by changing the discontinuity vector at the source depth to that given in (A36). Using the same notation as O'Toole & Woodhouse (2011), we write the discontinuity vectors explicitly as

$$\mathbf{s}_m^{\text{p-SV}} = \begin{cases} \begin{bmatrix} \frac{F_3}{\sigma} \\ -\frac{k(\sigma(M_{11}+M_{22})-2(\lambda+\mu)M_{33})}{2\mu\sigma} \\ -\frac{1}{2}k^2(M_{11}+M_{22}) + \frac{(k^2\lambda+\rho\omega^2)M_{33}}{\sigma} \\ -\frac{k\lambda F_3}{\sigma} \end{bmatrix} & m = 0 \\ \begin{bmatrix} \frac{k}{2\mu\sigma}((\lambda+\mu)(\mp M_{13}+iM_{23})+\mu(\pm M_{31}-iM_{32})) \\ \frac{1}{2\mu}(\pm F_1-iF_2) \\ \frac{1}{2}k(\pm F_1-iF_2) \\ \frac{1}{2\sigma} \left[k^2\lambda(\mp M_{31}+iM_{32}) + \frac{1}{\mu}(\pm M_{13}-iM_{23})(k^2(\lambda\mu-(\gamma+\mu)\sigma+\rho\sigma\omega^2)) \right] \end{bmatrix} & m = \pm 1 \\ \begin{bmatrix} 0 \\ \frac{1}{4\mu}k(M_{11}-M_{22}) \mp \frac{1}{4\mu}ik(M_{12}+M_{21}) \\ \frac{1}{4}k^2(M_{11}-M_{22}) \mp \frac{1}{4}ik^2(M_{12}+M_{21}) \\ 0 \end{bmatrix} & m = \pm 2 \end{cases} \quad (\text{A37})$$

and

$$\mathbf{s}_m^{\text{SH}} = \begin{cases} \begin{bmatrix} \frac{k}{2\mu}(-M_{12}+M_{21}) \\ 0 \end{bmatrix} & m = 0 \\ \begin{bmatrix} \frac{1}{2\mu}(\mp F_2-iF_1) \\ \frac{1}{2\mu}(k^2\mu-\rho\omega^2)(\pm M_{23}+iM_{13}) \end{bmatrix} & m = \pm 1 \\ \begin{bmatrix} \frac{-k}{4\mu}(M_{12}+M_{21}) \pm \frac{ik}{4\mu}(M_{22}-M_{11}) \\ 0 \end{bmatrix} & m = \pm 2 \end{cases} \quad (\text{A38})$$